

## Article

# Deep Learning on Synthesized Sensor Characteristics and Transmission Spectra Enabling MEMS-Based Spectroscopic Gas Analysis Beyond the Fourier Transform Limit

Samar Elaraby <sup>1,†</sup> , Sherif M. Abuelenin <sup>1,\*</sup> , Adel Moussa <sup>1,2</sup> and Yasser M. Sabry <sup>3,4</sup> 

<sup>1</sup> Department of Electrical Engineering, Faculty of Engineering, Port Said University, Port Fouad, Port Said 42526, Egypt; samar.elaraby@eng.psu.edu.eg (S.E.); amelsaye@ucalgary.ca (A.M.)

<sup>2</sup> Geomatics Department, Schulich School of Engineering, University of Calgary, Calgary, AB T2N 1N4, Canada

<sup>3</sup> Faculty of Engineering, Ain Shams University, Cairo 11535, Egypt; yasser.sabry@eng.asu.edu.eg

<sup>4</sup> Optical MEMS Technology Business Unit, Si-Ware Systems, Cairo 11361, Egypt

\* Correspondence: s.abuelenin@eng.psu.edu.eg; Tel.: +20-100-536-5313

† Samar Elaraby contributed to this work while was with Port Said University.

**Abstract:** Miniaturized Fourier transform infrared spectrometers serve emerging market needs in many applications such as gas analysis. The miniaturization comes at the cost of lower performance than bench-top instrumentation, especially for the spectral resolution. However, higher spectral resolution is needed for better identification of the composition of materials. This article presents a convolutional neural network (CNN) for 3X resolution enhancement of the measured infrared gas spectra using a Fourier transform infrared (FTIR) spectrometer beyond the transform limit. The proposed network extracts a set of high-dimensional features from the input spectra and constructs high-resolution outputs by nonlinear mapping. The network is trained using synthetic transmission spectra of complex gas mixtures and simulated sensor non-idealities such as baseline drifts and non-uniform signal-to-noise ratio. Ten gases that are relevant to the natural and bio gas industry are considered whose mixtures suffer from overlapped features in the mid-infrared spectral range of 2000–4000  $\text{cm}^{-1}$ . The network results are presented for both synthetic and experimentally measured spectra using both bench-top and miniaturized MEMS spectrometers, improving the resolution from 60  $\text{cm}^{-1}$  to 20  $\text{cm}^{-1}$  with a mean square error down to  $2.4 \times 10^{-3}$  in the transmission spectra. The technique supports selective spectral analysis based on miniaturized MEMS spectrometers.

**Keywords:** FTIR spectroscopy; MEMS spectrometer; infrared gas analyzer; superresolution; deep learning; convolutional neural-network



**Citation:** Elaraby, S.; Abuelenin, S.M.; Moussa, A.; Sabry, Y.M. Deep Learning on Synthesized Sensor Characteristics and Transmission Spectra Enabling MEMS-Based Spectroscopic Gas Analysis Beyond the Fourier Transform Limit. *Foundations* **2021**, *1*, 304–317. <https://doi.org/10.3390/foundations1020022>

Academic Editors: Cristina Achim, Ana Bratu, Mioara Petrus and Francesco Carlo Morabito

Received: 1 September 2021

Accepted: 12 December 2021

Published: 15 December 2021

**Publisher's Note:** MDPI stays neutral with regard to jurisdictional claims in published maps and institutional affiliations.



**Copyright:** © 2021 by the authors. Licensee MDPI, Basel, Switzerland. This article is an open access article distributed under the terms and conditions of the Creative Commons Attribution (CC BY) license (<https://creativecommons.org/licenses/by/4.0/>).

## 1. Introduction

Infrared spectroscopy is the science and technology of identifying and quantifying the composition of matter based on the interaction of their molecular vibrations and rotations with the light in the infrared region of the spectrum [1,2]. It is serving a huge number of applications in different domains such as the biological, pharmaceutical, chemical, food and beverage and environmental monitoring industries. One example is the infrared gas analyzers that can serve natural gas analyses, air quality monitoring, threat or gas leakage detection and medical diagnostics [3,4]. The market is growing fast and is expected to grow even faster due to the introduction of the miniaturized spectrometers enabling portability and ubiquitous spectral sensing for both professional and consumer use [5].

Different miniaturization or microscale technologies have emerged to serve the existing market and open new markets, such as microelectromechanical systems (MEMS) Fourier transform infrared (FTIR) spectrometers [6,7], tunable selective filter spectrometers [8], linear variable filters [9] and dispersive grating spectrometers [10]. The miniaturization comes at the cost of lower performance than bench-top instrumentation, especially

for the spectral resolution. In FTIR spectrometers, the resolution is limited by the travel range of the micromirror of the scanning Michelson interferometer following the uncertainty principle [1,11]  $\Delta x \Delta \nu \sim 1$ , where  $\Delta x$  is full travel range of the mirror and  $\Delta \nu$  is the spectral resolution in the wavenumber domain. The resolution in the wavelength domain  $\Delta \lambda = \Delta \nu \lambda^2$ , where  $\lambda$  is the wavelength. For resonance filter-based techniques, high reflectivity mirrors together with a longer physical cavity are needed to achieve fine spectral resolution but this forces the filter to operate at high-resonance, thus limiting the spectral range of operation [12]. Finally, for first diffraction order dispersive grating spectrometers, the resolution follows the relation  $\Delta \lambda N = \lambda$  [13] where  $N$  is the number of grooves on the diffraction grating. This is consistent with the transform limit theory stating that the smallest resolvable unit transform is inversely proportional to the number of samples.

Multivariate analysis, sometimes referred to as chemometrics, is usually used to predict the concentration of the different compositions of the sample [1]. The accuracy of prediction depends on many factors such as the ratio between signal and noise, spectral resolution, accuracy of the  $x$ -axis (i.e., wavelength accuracy) and the accuracy of the  $y$ -axis (i.e., photometric accuracy). In the case of gas analysis, spectral resolution is of particular importance. Therefore, there is a need for realizing a high-resolution spectral analysis over a wide spectral range based on a compact spectroscopic device. Higher (finer) spectral resolution is required for better identification and quantification of materials. In fact, the resolution plays an important role in the ability of material identification and sometimes the sensitivity to lower concentration as well [1,14]. One notable example for smart industry is the analysis of the biogas and natural gas contents as a primary source of energy in domestic and industrial markets. On one hand, this kind of gas is composed of a mixture of compounds whose spectral fingerprint is spread over a wide spectral range as shown in Figure 1. On the other hand, the various hydrocarbons in such gases (e.g.,  $\text{CH}_4$ ,  $\text{C}_2\text{H}_6$ ,  $\text{C}_3\text{H}_8$ ,  $\text{C}_4\text{H}_{10}$ ) have a similar molecular structure requiring selective detection (fine resolution).

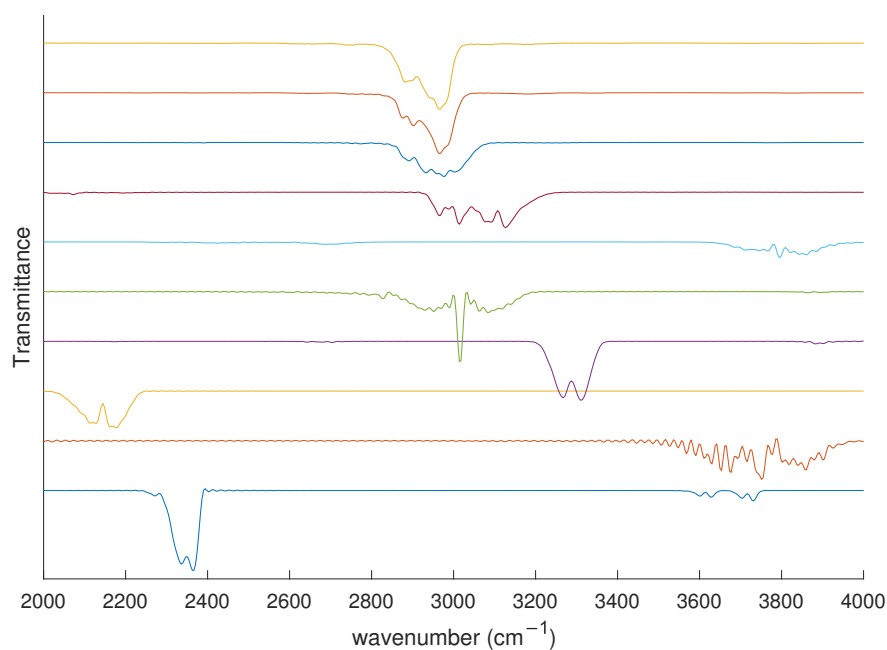


**Figure 1.** Transmittance of the 10 gases used in this study, with spectral resolution of  $60 \text{ cm}^{-1}$ . Spectra are shifted and scaled in the  $y$ -axis for clarity. Gases are (from below going up):  $\text{CO}_2$ ,  $\text{H}_2\text{O}$ ,  $\text{CO}$ ,  $\text{C}_2\text{H}_2$ ,  $\text{CH}_4$ ,  $\text{H}_2\text{S}$ ,  $\text{C}_2\text{H}_4$ ,  $\text{C}_2\text{H}_6$ ,  $\text{C}_3\text{H}_8$ , and  $\text{C}_4\text{H}_{10}$ .

Therefore, there is a need for realizing a high-resolution spectral analysis over a wide spectral range based on compact spectroscopic devices. To this end, several infrared spectroscopy

resolution enhancement techniques have been reported from, on one hand, by innovative hardware architectures together with the corresponding signal processing [15–17] and, on the other hand, by using signal processing techniques on the conventional hardware such as auto-regression [18] and compressed sensing [19]. However, the offered resolution enhancement of such techniques is still not enough compared to the resolution of bench-top devices, and is accompanied with spectral distortion necessitating the need for incorporating new directions. Deep learning (DL) was shown to be very successful in resolution enhancement of different types of signals, such as images [20,21], medical imaging [22], interferometry [23], fluorescence microscopy [24,25], field-emission scanning electron microscopy [26], magnetic resonance imaging (MRI) [27], and vascular ultrasound imaging [28]. DL was also applied in enhancement of other one-dimensional (1D) signals such as speech [29,30].

In this article, we use a deep convolutional neural network (CNN) for virtual resolution enhancement of FTIR gas spectra. The article extends and further improves previously presented results [31]. The neural network considers the low-resolution spectrum as the input and generates a high-resolution one. In [31], a CNN was introduced as a proof-of-concept to enhance the resolution of gas spectra that are composed of mixtures of different percentages of six gases. We extend the results by considering mixtures of ten gases that are relevant to the gas industry. The consideration of extra gases poses an extra problem, which is the overlapping of spectral peaks of different gases. The neural-network parameters have to be carefully tuned to be able to resolve such overlapped peaks. Additionally, the previously reported problem of false peaks in the enhanced spectra was improved in the work presented here. Finally, we extend the results by enhancing the resolution of experimentally measured spectra using both bench-top FTIR spectrometer (bench-top device Tensor II by Bruker) and a miniaturized mid-infrared MEMS FTIR spectrometer [32]. The training of the CNN required the consideration of data with different spectral resolutions and signal-to-noise ratios (SNRs). Other features in the data have also been accounted for, as discussed in detail below.

The rest of the article is structured as follows. Section 2 discusses the methodology of datasets synthesis, the network architecture and the training process. In Section 3, we show the results of the trained network and evaluate the performance of the proposed network with synthetic and measured data. Conclusions are presented in Section 4.

## 2. Methodology

Generally, resolution enhancement methods apply signal processing techniques on the low-resolution input signal to reach a higher resolution version (e.g., [33,34]). These signal processing techniques mainly adopt either a local or global approach to generate the missing samples needed to enhance the resolution. Interpolation based techniques approaches are mainly dominated by the neighbor samples or hand crafted features to deduce the missing samples; such a step does not directly benefit from potential useful characteristics of the whole signal. On the other hand, frequency based enhancement approaches inject the required information based on a theoretical assumption and ignore the local information around each sample.

CNN architecture enables the processing of the input signal on different layers, where the signal is convolved with many kernels to capture local features around each sample, the output of each layer is fed to the next level to capture more abstract features as wider neighborhood of the sample is involved. Finally, fully connected layers enable the involvement of the whole signal to affect each output sample. The convolution kernels at each layer and the weights at fully connected layers are initiated randomly and modified iteratively through the learning process, where the output signal is kept closer to the ground truth of the corresponding input. This CNN architecture enables both local features around samples and global features of the whole signal to be employed in the enhancement process. Instead of adopting theoretical assumptions about the signal, CNN uses the training data (input low-resolution signals and corresponding ground truth high-resolution versions) to adjust the kernels and weights and to extract features and to implicitly learn the required

mapping based on realistic data which provides a superior performance when compared with traditional approaches.

In this research, CNN is proposed for the FTIR resolution enhancement problem. Training the proposed neural network requires the availability of large sets of low- and high-resolution gas spectra, where the high-resolution spectra are considered as ground-truth. Experimentally acquiring such large sets of data is very challenging. Therefore, we relied on generating synthetic spectra that imitates the measured spectra. The network was trained using the synthesized low- and high-resolution data. The details of the training data set and the employed synthesis is covered in Section 2.1 and the network architecture is discussed in Sections 2.2 and 2.3.

### 2.1. Training Datasets

For training the neural network, a very large set of high- and low-resolution gas spectra was utilized at different SNRs. The utilized data of gas spectra were synthesized using data available from both the spectroscopic HITRAN (high-resolution transmission molecular absorption database) online database [35] and database generated by Pacific Northwest National Laboratory (PNNL) [36]. Each generated spectrum represents a mixture of different amount of gases that are relevant to the gas industry, namely, Carbon dioxide CO<sub>2</sub>, water vapor H<sub>2</sub>O, Carbon monoxide CO, Acetylene C<sub>2</sub>H<sub>2</sub>, Methane CH<sub>4</sub>, Hydrogen sulfide H<sub>2</sub>S, Ethene (Ethylene) C<sub>2</sub>H<sub>4</sub>, Ethane C<sub>2</sub>H<sub>6</sub>, Propane C<sub>3</sub>H<sub>8</sub>, and Butane C<sub>4</sub>H<sub>10</sub>. PNNL provides the absorption for a sample concentration of one part-per million (ppm) in one-meter optical path length at 296 kelvins, and HITRAN provides a compilation of spectroscopic parameters that are used by a set of computer codes to predict and simulate the transmission and emission of light in gases. The amount of gases in the synthesized mixtures were limited to percentages that are relevant to the mentioned industrial applications.

### Synthesis of Different Resolution Spectra

The spectra obtained from HITRAN and PNNL are of high-resolution. Creating spectra with lower resolutions was performed as follows. Spectral resolution depends directly on the maximum optical path difference (OPD) that can be measured by the spectrometer [1,37]. To simulate the effect of lower resolution FTIR spectrometers, a model based on a Michelson interferometer was used for interferogram calculation taking into consideration the limited OPD. Given the absorptivity of gases, the input spectrum (transmittance)  $S_{in}(v)$  is calculated based on Beer-Lambert law,

$$S_{in} = e^{-\epsilon(v)CL}, \quad (1)$$

where  $\epsilon$  is the gas absorptivity,  $C$  is the gas concentration and  $L$  is the path length. The interferogram  $I(x)$  is then calculated using the following equation, neglecting the dispersion effect

$$I(x) = \int_{v_1}^{v_2} S_{in}(v) \cos(2\pi vx) dv, \quad (2)$$

where  $x$  is the optical path difference between interferometer arms,  $v_1$  and  $v_2$  are minimum and maximum wavenumbers. Then, the output gas spectrum  $S_{out}(v)$  is calculated using Fourier transform of the interferogram as follows

$$S_{out}(v) = \int_{-OPD}^{OPD} I(x) \cos(2\pi vx) dx, \quad (3)$$

The resulting spectrum resolution is calculated as  $0.604/OPD$  [1]. For synthesizing the two sets of data (low- and high-resolution) used in our work, the corresponding interferograms were generated and truncated to maximum OPDs of 0.01 and 0.03 m, respectively. Applying FFT to the interferograms resulted in spectra of resolutions 60 and  $20 \text{ cm}^{-1}$ . Next, different values of signal-to-noise ratios (SNRs) were considered in the data.

The effect of the SNR was included by adding additive white Gaussian noise (AWGN) to the interferograms. The SNR is defined as [38]

$$\text{SNR (dB)} = 10 \log\left(\frac{1}{N_{rms}}\right), \tag{4}$$

where  $N_{rms}$  is the rms value of the added AWGN. Figure 2 shows an example of the low- and high-resolution data.

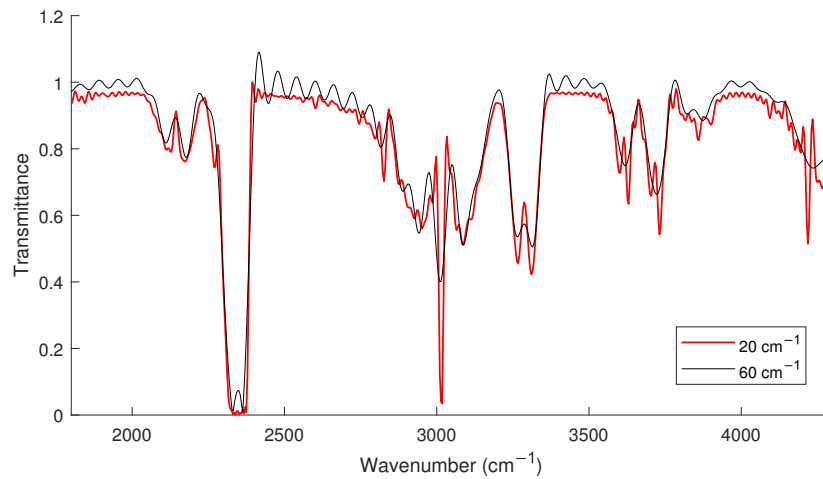


Figure 2. An example of low- and high-resolution spectrums of a gas mixture.

In order to avoid possible sources of overfitting of the neural network, different random number generating methods were used in generating the noise. Additionally, to induce variability in the training dataset, additional sets were added to the low-resolution (input) training data with different OPDs.

### 2.2. The Proposed Convolutional Neural Network

In this section, we propose a CNN for the FTIR resolution enhancement problem. The CNN structure is shown in Figure 3. It consists of four layers: two convolutional and two fully-connected layers. The given dataset contains low-resolution spectrums and their associated high-resolution versions, denoted by  $X$  and  $Y$ , respectively. The network is trained to learn a function  $F$  that maps between the low- and high-resolution spectra, such that the discrepancy between  $F(X)$  and  $Y$  is minimized. In the following, we describe the network architecture and the training process.

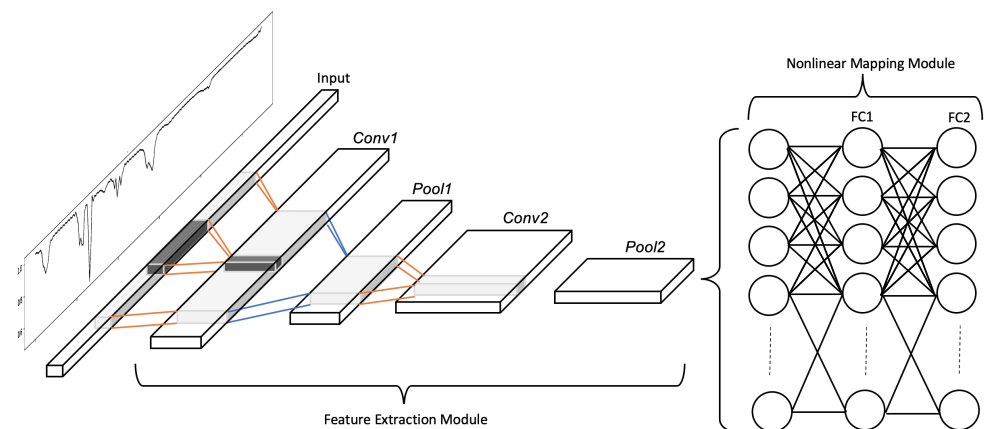


Figure 3. The proposed 1D CNN architecture with two convolutional and two fully-connected layers.

### 2.3. Network Architecture

The proposed network includes two convolutional layers that extract a set of high-dimensional features from the input spectra. These extracted features are fed into two fully connected layers that serve as a nonlinear mapping that constructs a high-resolution output spectrum through the training process. The number of input and output neurons are equal to the number of samples in the input and output spectra, respectively.

#### 2.3.1. Feature Extraction Layers

The feature extraction is achieved using two convolutional layers, each of which is followed by a pooling layer. At each convolutional layer, the input is convolved by  $K_l$  trainable kernels in order to extract  $K_l$  feature maps at the layer output  $\mathbf{X}^{[l]}$ . The superscript in the following refers to the layer number where  $\mathbf{X}^{[0]} = \mathbf{X}$ . The kernel size at the  $l^{th}$  layer is  $K_{l-1} \times 1 \times F_l$ . The  $n^{th}$  feature map can be expressed as

$$\mathbf{X}_n^{[l]} = \sigma_l \left( \sum_{k=1}^{K_{l-1}} \theta_{k,n}^{[l]} * \mathbf{X}_k^{[l-1]} \right), \tag{5}$$

where  $*$  is the 1D-convolution operator,  $\sigma_l$  a point-wise activation function, and  $\theta_{k,n}^{[l]} \in \mathbb{R}^{1 \times F_l}$  the kernel trainable weights with  $k = 1, \dots, K_{l-1}$ . The function of the pooling layer, applied to the output of each convolutional layer, is twofold. First, it is used to reduce the dimension of the extracted features, and accordingly, the computational complexity. Second, it quickly expands the kernel reach when we go deep in the network. Accordingly, the first layer, *conv1*, learns an arbitrary set of local features of the low-resolution spectra. However, the second layer *conv2* involves more samples from the input spectrums and becomes able to extract global features. The kernel reach of the two layers is highlighted in Figure 3 with dark and light gray boxes, respectively.

#### 2.3.2. Nonlinear Mapping Layers

The final nonlinear mapping is achieved using two fully-connected layers, *FC1* and *FC2*, to map the extracted features into a high-resolution spectrum. The output of each layer is given by

$$\mathbf{X}^{[l]} = \sigma_l \left( \mathbf{W}^{[l]} \circ \mathbf{X}^{[l-1]} \right), \tag{6}$$

where the operator  $\circ$  is the matrix multiplication, and  $\mathbf{W}^{[l]}$  contains the trainable weights of the  $l^{th}$  layer. The non-linearity is introduced by the nonlinear activation function  $\sigma_l$  used at each layer. The activation function used in all layers in this work is the Rectified Linear Unit (ReLU).

#### 2.3.3. Loss Function

The network is trained to estimate the trainable weights that minimize a pre-defined loss function. We define the loss function as the mean square error (MSE) between the predicted spectrum  $F(\mathbf{X}_i)$  and the ground-truth spectrum  $\mathbf{Y}_i$ :

$$L(\Theta) = \frac{1}{N} \sum_{i=1}^N \|F(\mathbf{X}_i; \Theta) - \mathbf{Y}_i\|_2^2, \tag{7}$$

where the subscript  $i$  refers to the  $i^{th}$  example in the training dataset, and  $N$  is the total number of spectrums in the dataset. Moreover,  $\Theta$  is a set of all trainable weights in the network that should be optimally chosen to minimize the loss function. In our experiments, we use the Adam algorithm to solve the minimization problem.

## 3. Synthetic and Experimental Results and Discussion

Without loss of generality, we execute experiments to scale up the resolution of the gas spectra from  $60 \text{ cm}^{-1}$  to  $20 \text{ cm}^{-1}$ . The range of wavelengths of our interest (relevant to

the miniaturized FTIR spectrometers [39]) falls between 2000 and 4000  $\text{cm}^{-1}$ . This range of wavenumbers was chosen based on the supported range of the miniature MEMS FTIR device and based on the application under study related to the group of gases of interest for natural gas, biogas analysis and environmental monitoring. Infrared gas analysis with smaller wavenumbers can be needed in other applications such as industrial process control and medical diagnostics [40].

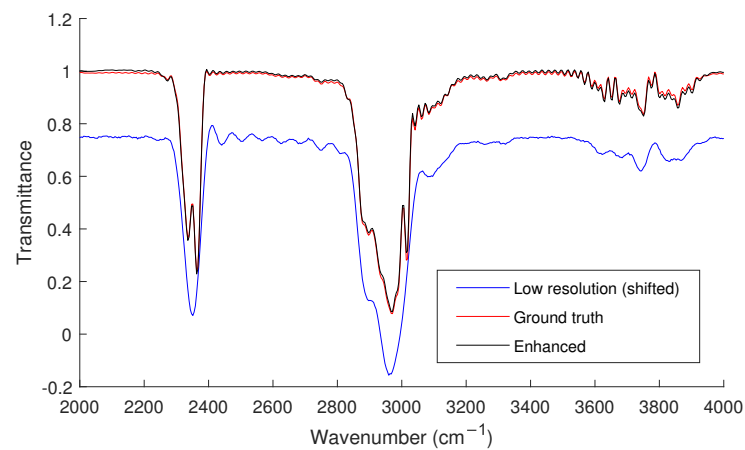
The training input and output spectra are accordingly limited to this range. A fixed number of samples is selected for both input and output spectra. Each spectrum is represented in exactly 520 discrete points (samples). One example is shown in Figure 2. The training and validation datasets have 70,000 and 8000 synthetic spectrums, respectively, generated as described in Section 2.1, at the two defined resolutions. The SNR used in the datasets ranges from 20 to 40 dB. Feature normalization is the only pre-processing step executed before training the network. The CNN hyper-parameters are set to the values shown in Table 1. We use 1D average pooling in *Pool1* and *Pool2* layers, which averages out each patch of two and four elements, respectively. The network is trained for 100 epochs using the Adam algorithm with a learning rate of  $10^{-3}$  and a weight decay of  $10^{-2}$ . The trained network is examined with both a synthetic dataset and real spectra measured using both a bench-top device and MEMS FTIR spectrometers.

**Table 1.** Convolutional Neural Network hyper-parameters.

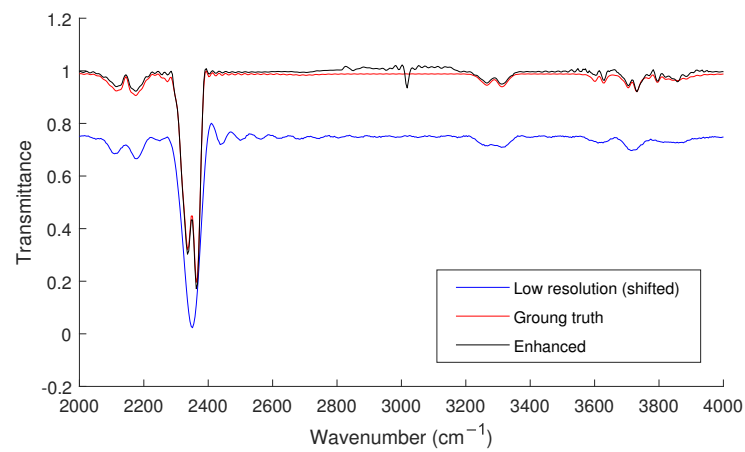
Hyper-Parameters	conv1	conv2	FC1	FC2
$K_l$	32	64	-	-
$F_l$	7	11	-	-
Stride	1	2	-	-
Padding	3	5	-	-
Pooling	Avg2	Avg4	-	-
Batch Normalization	N	N	Y	Y
Dropout	-	-	0.5	0.5
Activation	Relu	Relu	Relu	Relu
No. of neurons	-	-	2048	4000

### 3.1. Synthetic Data

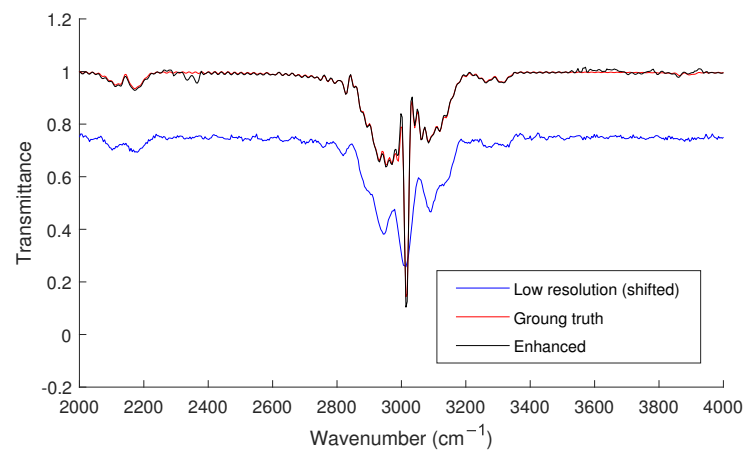
We first tested the trained data with a synthetic dataset of another 8000 synthesized spectrums. The test loss, calculated as in (7), was  $1.2 \times 10^{-4}$ . Figure 4 shows the output of the trained CNN for two different examples of the test data. The network was able to construct the high-resolution spectrum with an average MSE identical to the test loss. The low-resolution (input) spectra in the figures was shifted by an amount of 0.25 for the sake of clarity. As can be seen from the figures, overall, the trained network performs well in resolving the overlapped peaks from the low-resolution spectra. As shown in Figure 4b,c, in some cases, (specially for lower SNR values), the noise in the low-resolution spectra are misidentified as peaks with small amplitude (e.g., the peak at  $\sim 3000\text{-cm}^{-1}$  in Figure 4b and the peak around  $\sim 2350\text{-cm}^{-1}$  in Figure 4c). The MSEs of these three examples were  $1.3 \times 10^{-4}$ ,  $2.2 \times 10^{-4}$ , and  $5.7 \times 10^{-5}$ , respectively.



(a)



(b)



(c)

**Figure 4.** Predicted high-resolution spectra from the synthetic low-resolution versions and the high-resolution spectra (ground truth), (the low-resolution spectra are shifted in the  $y$ -axis for clarity) for different gas mixtures measured at different SNRs: (a) mixture of  $\text{CO}_2$  (4.2%),  $\text{H}_2\text{O}$  (10%),  $\text{C}_2\text{H}_2$  (0.7%),  $\text{CH}_4$  (21.7%),  $\text{H}_2\text{S}$  (40.7%),  $\text{C}_2\text{H}_4$  (1.2%),  $\text{C}_2\text{H}_6$  (7.6%),  $\text{C}_2\text{H}_8$  (6.8%), and  $\text{C}_2\text{H}_{10}$  (7.2%) at  $\text{SNR} = 34.5$  dB, (b) mixture of  $\text{CO}_2$  (5%),  $\text{CO}$  (3.9%),  $\text{C}_2\text{H}_2$  (1.4%), and  $\text{H}_2\text{S}$  (89.7%) at  $\text{SNR} = 28.8$  dB, (c) mixture of  $\text{CO}$  (2.6%),  $\text{C}_2\text{H}_2$  (1.1%),  $\text{CH}_4$  (89.4%),  $\text{C}_2\text{H}_4$  (3.3%) and  $\text{C}_2\text{H}_6$  (3.7%) at  $\text{SNR} = 23.7$  dB.

### 3.2. Experimental Measurements

The synthetic data show the theoretical gas spectra; however, the measured spectra are affected by many background distractors, such as light sources and the gases in the surrounding atmosphere resulting in distortions in the measured spectrum. Additionally, other artifacts and nonlinearities affect the measured spectra from different devices. This includes non-constant baselines. Theoretical transmission spectra have all the spectral peaks ‘dropped’ from horizontal baselines while the baselines of the measured spectra are affected by the device and the orientation of the gas cell, which cause them to have tilted baselines (see [41] and the figures therein). Additionally, non-uniform SNR commonly occur in miniaturized MEMS spectrometers, where the noise affects some wavelengths more than others. Also, the shape of the apodization function is another source of artifacts in the measured spectra. In this subsection, we discuss the performance of the trained network with real measurements. For the experiment, we measured the spectrum of a cell that contains a mixture of CO<sub>2</sub> (0.25%), CO (4%), CH<sub>4</sub> (1.2%) and H<sub>2</sub>S (94.5%) using both the bench-top device and a mid-infrared MEMS FTIR spectrometer at a resolution of 60 cm<sup>-1</sup>. The details of the measurement was as follows. A 10-cm length free-space gas cell filled with the gas mixture and sealed was specially ordered (from Wavelength References). The pressure inside the cell is the atmospheric pressure. The cell has wedged MgF<sub>2</sub> windows transparent in the wavelength range of interest. The diameter of the cell is about 25 mm. The cell was measured using the setup shown in the schematic in Figure 5a, while a photo for the real setup is shown in Figure 5b with the light source switched on. An infrared light source (Thorlabs, HEP3965) was used. The light is collimated and focused using CaF<sub>2</sub> lenses (Thorlabs) by placing them at a distance equal to their focal length away from the source and spectrometer input. A measurement background is taken while the two lenses are in close proximity. Then the gas cell is inserted and measured referenced to the background.

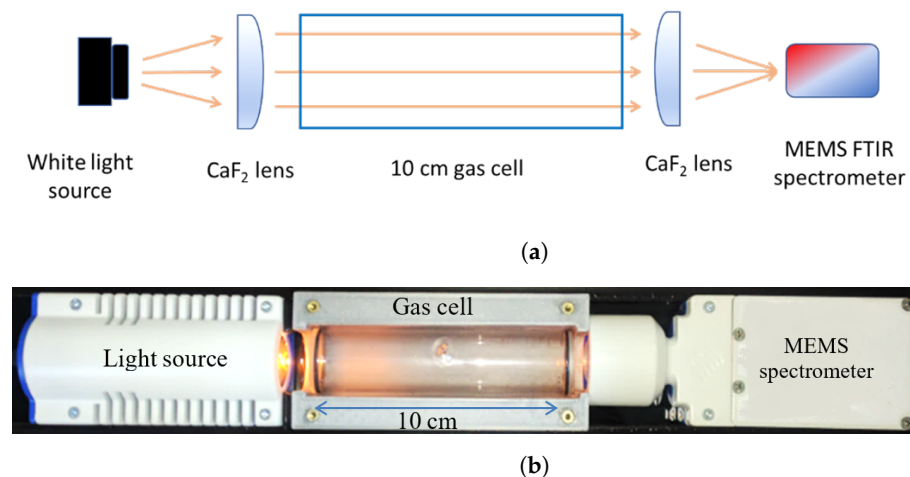


**Figure 5.** Gas cell measurement setup; (a) schematic diagram, (b) photo of the real setup with the light source turned on.

Next, the measured spectra went through two pre-processing steps. First, we followed the algorithm of [41] in order to correct the baseline of the measured spectrum. The second pre-processing step is re-sampling. Commonly, down-sampling process has to be executed as the measured spectrum is usually represented in more than 520 samples (the number of inputs to the CNN). Figure 6 depicts both the synthetic low-resolution and measured spectrums of the same cell using both bench-top device and MEMS FTIR spectrometers. The bench-top device measured spectrum is shown after baseline removal, as mentioned above. As the figure shows, even after baseline removal, there is still some discrepancy between the theoretical and measured spectra; this is expected to affect the performance of the trained network in resolving real measurements. Moreover, the spectrum measured

using the MEMS FTIR spectrometer shows further differences compared to the other two spectra, as it is affected by the other factors mentioned above.

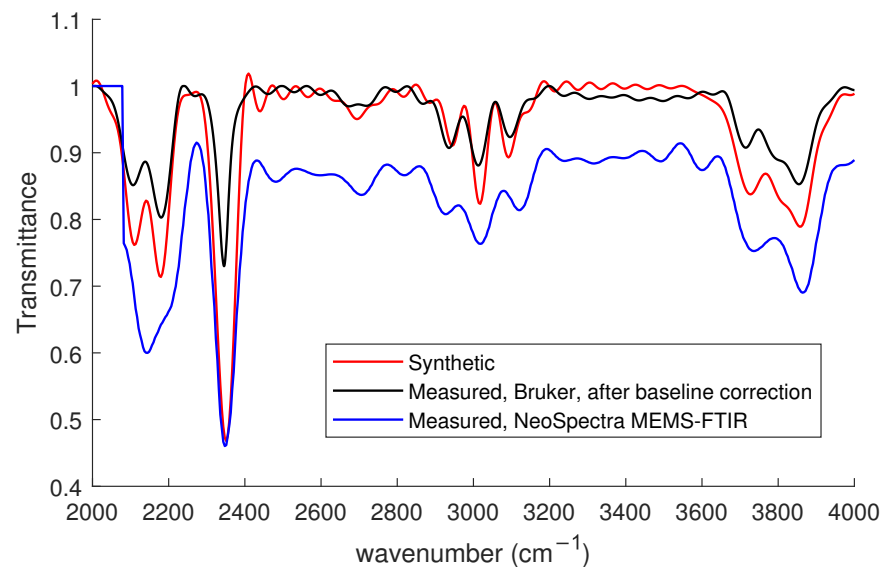


**Figure 6.** Synthetic and measured spectra of the experimental gas cell at a resolution of  $60\text{ cm}^{-1}$ . Measurements were performed using both bench-top (Bruker Tensor II) and MEMS-FTIR (NeoSpectra) devices. The gas cell measured contains  $\text{CO}_2$  (0.25%),  $\text{CO}$  (4%),  $\text{CH}_4$  (1.2%) and  $\text{H}_2\text{S}$  (94.5%).

### 3.2.1. Enhancing Bench-Top Spectrometer Measured Spectrum

The predicted high-resolution spectrum from the bench-top device measurement using the trained CNN is illustrated in Figure 7 (in blue-dashed line). The figure also shows the low-resolution measured spectrum. And for comparison, two high-resolution versions of the same spectrum are shown; a synthetic (theoretical ground truth) version that was constructed given the contents of the gas cell, and an experimental high-resolution version that was measured using the bench-top spectrometer.

We note here that there is amplitude discrepancy between the synthetic spectrum and the high-resolution measured spectrum (as well as the enhanced spectrum). This is mainly due to distortions in the measurement process. The major difference in peak amplitude is encountered around  $2400$  and  $3700\text{ cm}^{-1}$ , the location of Carbon dioxide peaks. This indicates that the measuring process was affected by some factors such as the  $\text{CO}_2$  in the atmosphere or the measuring setup itself. A CNN model that is trained over synthetic data would not be able to mitigate this effect.

The original CNN model recognized all the peaks of the spectrum and enhanced the resolution of the given low-resolution spectrum. The main discrepancy between the two spectra is the existence of a 'flipped' peak around  $3300\text{ cm}^{-1}$  in the predicted spectrum. This is mainly due to the difference between the measured and synthetic spectra as shown in Figure 6, which is mainly a baseline error that was not totally corrected in the pre-processing of the measured spectrum. This problem was mitigated by re-training the network with an extra set of synthetic data in which artificial baselines were induced. The new spectrum enhanced using the re-trained CNN is shown in the same figure in black solid line. In comparison to the synthetic spectrum, using the re-trained CNN has reduced the MSE of the enhanced spectrum from  $4.2 \times 10^{-3}$ , to  $3.5 \times 10^{-3}$ . The MSE between the enhanced spectrum and the high-resolution measurement is approximately  $2.75 \times 10^{-3}$ . The amplitude discrepancy between the predicted and measured high-resolution spectrum is lower than that between the predicted and the synthetic, therefore the error is lower. However, because the measured spectrum has to go through a baseline correction process, as explained above, and the baseline correction algorithm is not unique, a baseline error can be seen in the measured spectrum between wavenumber values of

3200 and 3600  $\text{cm}^{-1}$ , which would contribute to increasing the overall error between the measured and predicted spectra.

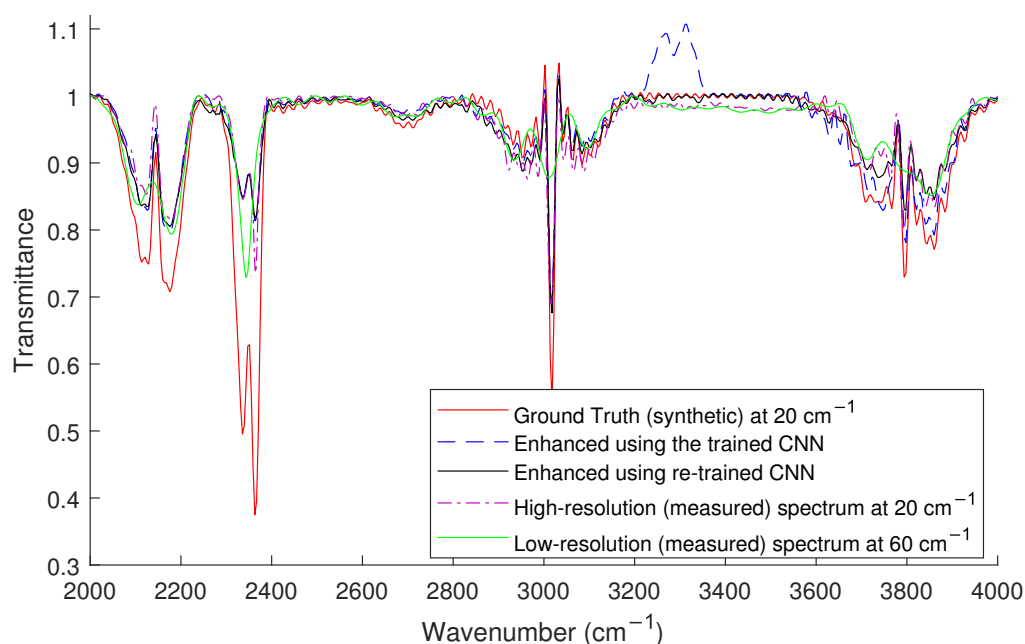


**Figure 7.** Predicted high-resolution spectrum (dashed-blue line) from a low-resolution measured spectrum (solid-green line) captured using a bench-top device spectrometer (Bruker). Also shown is the synthetic high-resolution spectrum and measured high-resolution spectrum of the same cell. The gas cell measured contains  $\text{CO}_2$  (0.25%),  $\text{CO}$  (4%),  $\text{CH}_4$  (1.2%) and  $\text{H}_2\text{S}$  (94.5%). The measured spectra are shown after pre-processing.

Moreover, in Figure 7, regardless of the overestimation of some peaks, all the peaks between 3600 and 4000  $\text{cm}^{-1}$  that are due to the overlapped spectra of  $\text{CO}_2$  and  $\text{H}_2\text{S}$  were resolved, even though not all of them appeared in the low-resolution measured spectrum. This comes as no surprise as the trained network relies on the global features of the spectra and was able to recognize the existence of both gases. This represents one example in which the influence of global features is desirable.

### 3.2.2. Enhancing MEMS FTIR Spectrometer Measured Spectrum

The predicted high-resolution spectrum from the MEMS FTIR measurement using the originally trained CNN is illustrated in Figure 8 (in blue dashed line) along with the ground-truth high-resolution spectrum.

Similar to the previously discussed case, the original CNN recognized all the peaks of the spectrum and enhanced the resolution of the given low-resolution spectrum. The main discrepancy between the two spectra was the existence of a 'flipped' peak around 3300  $\text{cm}^{-1}$  in the predicted spectrum. Again, this is due to the difference between the measured and synthetic spectra as shown in Figure 6. As discussed earlier, miniaturized MEMS FTIR spectrometers induce several effects on their measurements. Data that model these effects were added to the training process in different trials. The network performance showed improvement when re-trained with an extra set of synthetic data in which the effect of non-uniform SNR was modeled. The new enhanced spectrum is shown in the same figure in black solid line. The MSE of both enhanced spectra are  $4.7 \times 10^{-3}$ , and  $2.4 \times 10^{-3}$ , respectively. It is worth mentioning here that although the false peaks were not totally removed, the SNR in this case is better than the enhancement of the bench-top device's measurement compared to the synthetic spectra as discussed above, because the other peaks of the spectrum better match the synthetic ground truth. The reason can be seen when comparing the low-resolution measurements shown in Figure 6, where MEMS

FTIR measurement (due to the non-linearities of the device) is closer in amplitude to the theoretical spectrum of the content of the cell.

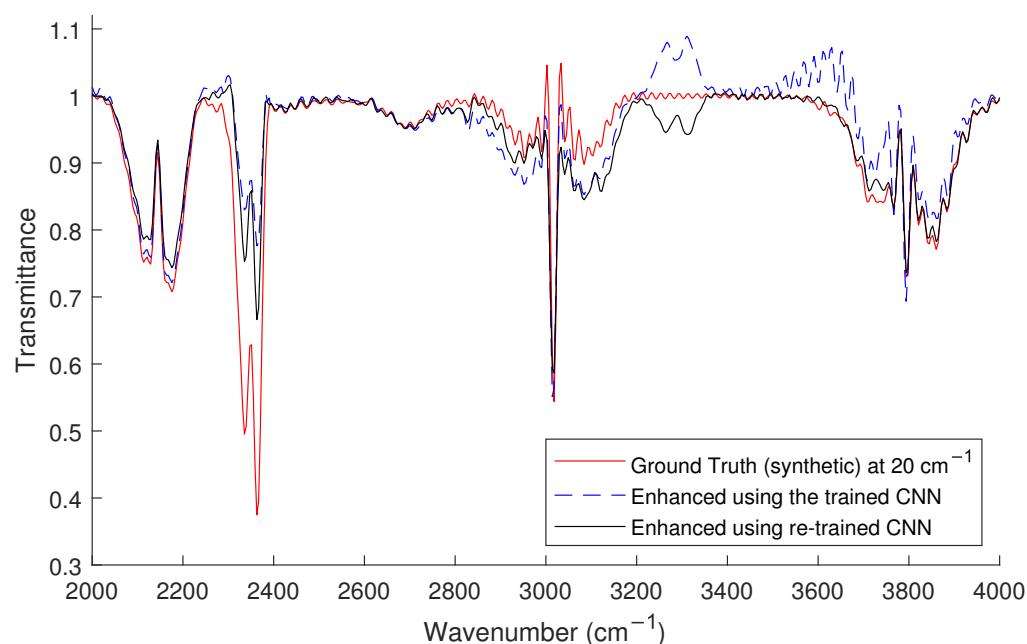


**Figure 8.** Predicted high-resolution spectrum from a measured spectrum captured using a MEMS FTIR spectrometer. The gas cell measured contains CO<sub>2</sub> (0.25%), CO (4%), CH<sub>4</sub> (1.2%) and H<sub>2</sub>S (94.5%). The measured spectrum is shown after pre-processing.

Since a mean square error down to  $2.4 \times 10^{-3}$  in the transmission spectra was obtained, it is expected that the error in production will be in that order. The exact values depend on the specific gas mixture concentrations and has to be calculated for case by case. Since the transmission  $T = \exp(-\epsilon CL)$ , one can deduce that the error in concentration is given by  $\Delta C = \Delta T[\epsilon L(1 - T)]^{-1}$ .

#### 4. Conclusions

While miniaturized Fourier transform infrared spectrometers are finding increasing numbers of important applications, such as gas analysis, they generally suffer from the problem of low spectral resolution. Higher spectral resolution is needed for better identification of materials. This article discussed a deep learning method for resolution enhancement of FTIR gas spectra. The proposed convolutional neural network can effectively enhance the low-resolution spectra by extracting a set of high-dimensional features from the input of low-resolution data and the constructing of high-resolution outputs. The network was trained using synthetic data and tested using both synthetic and measured spectra of gas mixtures. The proposed method was shown to result in better identification of the absorption peaks by producing a threefold resolution enhancement.

**Author Contributions:** Conceptualization, S.M.A. and S.E.; methodology, S.E. and A.M.; software, S.E.; validation, Y.M.S.; investigation, S.E. and S.M.A.; resources, Y.M.S.; data curation, Y.M.S.; writing—original draft preparation, S.E.; writing—review and editing, S.M.A., A.M. and Y.M.S.; visualization, S.E.; supervision, S.M.A. and Y.M.S.; project administration, S.M.A.; funding acquisition, S.M.A. All authors have read and agreed to the published version of the manuscript.

**Funding:** This work was supported in part by the Information Technology Academia Collaboration (ITAC) program, Egypt (Grant number CFP155).

**Institutional Review Board Statement:** Not applicable.

**Informed Consent Statement:** Not applicable.

**Data Availability Statement:** The data presented in this study are available on request from the corresponding author.

**Conflicts of Interest:** The authors declare no conflict of interest.

### Abbreviations

The following abbreviations are used in this manuscript:

AWGN	Additive White Gaussian Noise
CNN	Convolutional Neural Network
DL	Deep Learning
FTIR	Fourier Transform Infrared
MEMS	Micro-electromechanical Systems
MSE	Mean Squared Error
OPD	Optical Path Difference
ReLU	Rectified Linear Unit
SNR	Signal-to-Noise Ratio

### References

1. Griffiths, P.R.; De Haseth, J.A. *Fourier Transform Infrared Spectrometry*, 2nd ed.; John Wiley and Sons: Hoboken, NJ, USA, 2006; pp. 1–529. [CrossRef]
2. Thompson, J.M. *Infrared Spectroscopy*; CRC Press: Boca Raton, FL, USA, 2018; p. 156.
3. Hodgkinson, J.; Tatam, R.P. Optical gas sensing: A review. *Meas. Sci. Technol.* **2012**, *24*, 012004. [CrossRef]
4. Lakkis, S.; Younes, R.; Alayli, Y.; Sawan, M. Review of recent trends in gas sensing technologies and their miniaturization potential. *Sens. Rev.* **2014**, *34*, 24–35. [CrossRef]
5. Molecular Spectroscopy Market 2019 Global Industry Company Profile, Brief Analysis by Regions, Growth Prospects, Future Scope and Trends by Forecast 2026. Available online: <https://www.databridgemarketresearch.com/REPORTS/GLOBAL-MOLECULAR-SPECTROSCOPY-MARKET> (accessed on 1 January 2020).
6. Sabry, Y.M.; Hassan, K.; Anwar, M.; Alharon, M.H.; Medhat, M.; Adib, G.A.; Dumont, R.; Saadany, B.; Khalil, D. Ultra-compact MEMS FTIR spectrometer. In *Next-Generation Spectroscopic Technologies X*; Druy, M.A., Crocombe, R.A., Barnett, S.M., Profeta, L.T., Eds.; Anaheim, California, United States, International Society for Optics and Photonics (SPIE): Bellingham, DC, USA, 2017; Volume 10210, pp. 63–70. [CrossRef]
7. Eltagoury, Y.M.; Sabry, Y.M.; Khalil, D.A. All-Silicon Double-Cavity Fourier-Transform Infrared Spectrometer On-Chip. *Adv. Mater. Technol.* **2019**, *4*, 1900441. [CrossRef]
8. Milne, J.S.; Dell, J.M.; Keating, A.J.; Faraone, L. Widely tunable MEMS-based fabry—Perot filter. *J. Microelectromech. Syst.* **2009**, *18*, 905–913. [CrossRef]
9. Zhang, S.; Bin, W.; Xu, B.; Zheng, X.; Chen, B.; Lv, X.; San, H.; Hofmann, W. Mixed-gas CH<sub>4</sub>/CO<sub>2</sub>/CO detection based on linear variable optical filter and thermopile detector array. *Nanoscale Res. Lett.* **2019**, *14*, 1–9. [CrossRef]
10. Pügner, T.; Knobbe, J.; Grüger, H. Near-Infrared Grating Spectrometer for Mobile Phone Applications. *Appl. Spectrosc.* **2016**, *70*, 734–745. [CrossRef] [PubMed]
11. Hall, M. Resolution and uncertainty in spectral decomposition. *First Break* **2006**, *24*. [CrossRef]
12. Ayerden, N.P.; Wolffenbuttel, R.F. The miniaturization of an optical absorption spectrometer for smart sensing of natural gas. *IEEE Trans. Ind. Electron.* **2017**, *64*, 9666–9674. [CrossRef]
13. Palmer, C.; Loewen, E.G. *Diffraction Grating Handbook*; Newport Corporation: Irvine, CA, USA, 2005.
14. Erfan, M.; Sabry, Y.M.; Sakr, M.; Mortada, B.; Medhat, M.; Khalil, D. On-Chip Micro-Electro-Mechanical System Fourier Transform Infrared (MEMS FT-IR) Spectrometer-Based Gas Sensing. *Appl. Spectrosc.* **2016**, *70*, 897–904. [CrossRef]
15. El-Sayed, I.S.; Sabry, Y.M.; ElZeiny, W.E.; Badra, N.; Khalil, D.A. Transformation algorithm and analysis of the Fourier transform spectrometer based on cascaded Fabry-Perot interferometers. *Appl. Opt.* **2018**, *57*, 7225–7231. [CrossRef]
16. Shaheen, A.; Sabry, Y.M.; Khalil, D.A.M. Combined MEMS spectrometer based on Michelson interferometer and tunable filter for wideband selective operation. In Proceedings of the SPIE MOEMS and Miniaturized Systems XIX, San Francisco, CA, USA, 28 February 2020.
17. Sabry, Y.M.; Khalil, D.A.M.; Saadany, B.A. Fourier Transform Micro Spectrometer Based on Spatially-Shifted Interferogram Bursts. U.S. Patent 9,429,474, 30 August 2016.
18. Samir, I.; Sabry, Y.M.; Fathy, A.; Ghoname, A.O.; Badra, N.; Khalil, D.A. Autoregressive superresolution microelectromechanical systems Fourier transform spectrometer. *Appl. Opt.* **2019**, *58*, 6784–6790. [CrossRef]
19. Sanders, J.N. Compressed Sensing for Chemistry. Ph.D. Thesis, Harvard University, Cambridge, MA, USA, 2016.
20. Dong, C.; Loy, C.C.; He, K.; Tang, X. Image Super-Resolution Using Deep Convolutional Networks. *IEEE Trans. Pattern Anal. Mach. Intell.* **2016**, *38*, 295–307. [CrossRef] [PubMed]

21. Yang, W.; Zhang, X.; Tian, Y.; Wang, W.; Xue, J.H.; Liao, Q. Deep Learning for Single Image Super-Resolution: A Brief Review. *IEEE Trans. Multimed.* **2019**, *21*, 3106–3121. [[CrossRef](#)]
22. Li, Y.; Sixou, B.; Peyrin, F. A review of the deep learning methods for medical images super resolution problems. *IRBM* **2021**, *42*, 120–133. [[CrossRef](#)]
23. Lee, S.; Oh, O.; Kim, Y.; Kim, D.; Hussey, D.S.; Wang, G.; Lee, S.W. Deep learning for high-resolution and high-sensitivity interferometric phase contrast imaging. *Sci. Rep.* **2020**, *10*, 9891. [[CrossRef](#)] [[PubMed](#)]
24. Wang, H.; Rivenson, Y.; Jin, Y.; Wei, Z.; Gao, R.; Günaydin, H.; Bentolila, L.A.; Kural, C.; Ozcan, A. Deep learning enables cross-modality super-resolution in fluorescence microscopy. *Nat. Methods* **2019**, *16*, 103–110. [[CrossRef](#)]
25. Xiao, D.; Chen, Y.; Li, D.D.U. One-Dimensional Deep Learning Architecture for Fast Fluorescence Lifetime Imaging. *IEEE J. Sel. Top. Quantum Electron.* **2021**, *27*, 7000210. [[CrossRef](#)]
26. Gao, Z.; Ma, W.; Huang, S.; Hua, P.; Lan, C. Deep Learning for Super-Resolution in a Field Emission Scanning Electron Microscope. *Ai* **2019**, *1*, 1–9. [[CrossRef](#)]
27. Zhao, C.; Shao, M.; Carass, A.; Li, H.; Dewey, B.E.; Ellingsen, L.M.; Woo, J.; Guttman, M.A.; Blitz, A.M.; Stone, M.; et al. Applications of a deep learning method for anti-aliasing and super-resolution in MRI. *Magn. Reson. Imaging* **2019**, *64*, 132–141. [[CrossRef](#)]
28. Van Sloun, R.J.; Solomon, O.; Bruce, M.; Khaing, Z.Z.; Eldar, Y.C.; Mischi, M. Deep Learning for Super-resolution Vascular Ultrasound Imaging. In Proceedings of the ICASSP 2019-2019 IEEE International Conference on Acoustics, Speech and Signal Processing (ICASSP), Brighton, UK, 12–17 May 2019; pp. 1055–1059. [[CrossRef](#)]
29. Han, W.; Wu, C.; Zhang, X.; Sun, M.; Min, G. Speech enhancement based on improved deep neural networks with MMSE pretreatment features. In Proceedings of the 2016 IEEE 13th International Conference on Signal Processing (ICSP), Chengdu, China, 6–10 November 2016; pp. 1140–1145. [[CrossRef](#)]
30. Saleem, N.; Khattak, M.I. Deep Neural Networks for Speech Enhancement in Complex-Noisy Environments. *Int. J. Interact. Multimed. Artif. Intell.* **2020**, *6*, 84–90. [[CrossRef](#)]
31. Elaraby, S.; Sabry, Y.M.; Abuelenin, S.M. Super-resolution infrared spectroscopy for gas analysis using convolutional neural networks. In Proceedings of the Applications of Machine Learning 2020, (Online), CA, USA, 24 August–4 September 2020; International Society for Optics and Photonics (SPIE): Bellingham, DC, USA, 2020; Volume 11511.
32. NeoSpectra-MIR Platform. Available online: <https://www.neospectra.com/our-offerings/neospectra-mir-platform/> (accessed on 1 November 2020).
33. Wahab, M.F.; O'Haver, T.C.; Gritti, F.; Hellinghausen, G.; Armstrong, D.W. Increasing chromatographic resolution of analytical signals using derivative enhancement approach. *Talanta* **2019**, *192*, 492–499. [[CrossRef](#)] [[PubMed](#)]
34. Wahab, M.F.; Gritti, F.; O'Haver, T.C. Discrete Fourier transform techniques for noise reduction and digital enhancement of analytical signals. *TrAC Trends Anal. Chem.* **2021**, *143*, 116354. [[CrossRef](#)]
35. HITRAN. Available online: <http://hitran.iao.ru/molecule/simlaunch> (accessed on 8 May 2018).
36. Sharpe, S.W.; Johnson, T.J.; Sams, R.L.; Chu, P.M.; Rhoderick, G.C.; Johnson, P.A. Gas-Phase Databases for Quantitative Infrared Spectroscopy. *Appl. Spectrosc.* **2004**, *58*, 1452–1461. [[CrossRef](#)] [[PubMed](#)]
37. Li, J.; Lu, D.F.; Qi, Z.M. A Modified Equation for the Spectral Resolution of Fourier Transform Spectrometers. *J. Light. Technol.* **2015**, *33*, 19–24. [[CrossRef](#)]
38. Davis, S.P.; Abrams, M.C.; Brault, J.W. *Fourier Transform Spectrometry*; Academic Press: Cambridge, MA, USA, 2001.
39. Fathy, A.; Sabry, Y.M.; Amr, M.; Gnambodoe-Capo-chichi, M.; Anwar, M.; Ghoname, A.O.; Amr, A.; Saeed, A.; Gad, M.; Al Haron, M.; et al. MEMS FTIR optical spectrometer enables detection of volatile organic compounds (VOCs) in part-per-billion (ppb) range for air quality monitoring. In Proceedings of the MOEMS and Miniaturized Systems XVIII, San Francisco, CA, USA, 2–7 February 2019; International Society for Optics and Photonics (SPIE): Bellingham, DC, USA, 2019; Volume 10931.
40. Popa, D.; Udrea, F. Towards integrated mid-infrared gas sensors. *Sensors* **2019**, *19*, 2076. [[CrossRef](#)] [[PubMed](#)]
41. Shen, X.; Xu, L.; Ye, S.; Hu, R.; Jin, L.; Xu, H.; Liu, W. Automatic baseline correction method for the open-path Fourier transform infrared spectra by using simple iterative averaging. *Opt. Express* **2018**, *26*, A609. [[CrossRef](#)]